Behavioral/Cognitive

Multiple Intrinsic Timescales Govern Distinct Brain States in Human Sleep

Danna D. Lendner, 1,2 Jack J. Lin, 3,4 Pål G. Larsson, and Randolph F. Helfrich

¹Hertie Institute for Clinical Brain Research, University Medical Center Tübingen, Tübingen 72076, Germany, ²Department of Anesthesiology and Intensive Care Medicine, University Medical Center Tübingen, Tübingen 72076, Germany, ³Department of Neurology, UC Davis, Sacramento, California 95816, ⁴Center for Mind and Brain, UC Davis, Davis, California 95618, and ⁵Department of Neurosurgery, University of Oslo Medical Center, Oslo 0372, Norway

Human sleep exhibits multiple, recurrent temporal regularities, ranging from circadian rhythms to sleep stage cycles and neuronal oscillations during nonrapid eye movement sleep. Moreover, recent evidence revealed a functional role of aperiodic activity, which reliably discriminates different sleep stages. Aperiodic activity is commonly defined as the spectral slope χ of the 1/frequency (1/f^{χ}) decay function of the electrophysiological power spectrum. However, several lines of inquiry now indicate that the aperiodic component of the power spectrum might be better characterized by a superposition of several decay processes with associated timescales. Here, we determined multiple timescales, which jointly shape aperiodic activity using human intracranial electroencephalography. Across three independent studies (47 participants, 23 female), our results reveal that aperiodic activity reliably dissociated sleep stage-dependent dynamics in a regionally specific manner. A principled approach to parametrize aperiodic activity delineated several, spatially and state-specific timescales. Lastly, we employed pharmacological modulation by means of propofol anesthesia to disentangle state-invariant timescales that may reflect physical properties of the underlying neural population from state-specific timescales that likely constitute functional interactions. Collectively, these results establish the presence of multiple intrinsic timescales that define the electrophysiological power spectrum during distinct brain states.

Key words: 1/f neural activity; aperiodic activity; intracranial EEG; intrinsic neural timescales; propofol anesthesia; sleep physiology

Significance Statement

Sleep is characterized by prominent temporal regularities. In this study, we unveil a previously unrecognized principle that governs neural activity during human sleep. Our results shed light on the existence of a set of intrinsic timescales that fundamentally define the current state of the sleeping brain. These timescales serve as indicators of both physiological and functional interactions within the underlying neural population. Through pharmacological modulation, we differentiated state-specific functional interactions from state-invariant timescales, suggesting that the latter may reflect the inherent physical properties of the neural population at play.

Introduction

It has long been recognized that distinct temporal signatures delineate different brain states. Sleep follows multiple temporal regularities, ranging from circadian rhythms to sleep cycles to sleep

Received Jan. 24, 2024; revised July 22, 2024; accepted Aug. 7, 2024.

Author contributions: J.D.L. and R.F.H. designed research; J.D.L., J.J.L., P.G.L., and R.F.H. performed research; J.D.L., P.G.L., and R.F.H. contributed unpublished reagents/analytic tools; J.D.L. and R.F.H. analyzed data; J.D.L. and R.F.H. wrote the paper.

This work was supported by the German Research Foundation (DFG LE3863/2-1 to J.D.L and HE8329/2-1 to R.F.H.), the Hertie Foundation (Network for Excellence in Clinical Neuroscience, R.F.H.), the Jung Foundation for Research and Science (Ernst Jung Career Advancement Award in Medicine, R.F.H.), the Medical Faculty of the University of Tübingen (TüFF Habilitation program, J.D.L; JRG Plus program, R.F.H.), and the National Institutes of Health (U19NS107609, J.J.L.). We thank Jan Martini and Frank van Schalkwijk for their helpful feedback.

The authors declare no competing financial interests.

Correspondence should be addressed to Randolph F. Helfrich at randolph.helfrich@gmail.com.

https://doi.org/10.1523/JNEUROSCI.0171-24.2024

Copyright © 2024 the authors

oscillations (Rasch and Born, 2013; Nir and de Lecea, 2023). Slow oscillations (<1.25 Hz) or sleep spindles (12-16 Hz) characterize nonrapid eye movement (non-REM) sleep in humans and rodents, while theta activity (4-10 Hz) dominates rodent REM sleep. While these periodic signatures are highly conserved across species during non-REM sleep (van Schalkwijk et al., 2023), REM sleep remained a conundrum since human REM sleep exhibits wake-like, desynchronized ("paradoxical") electroencephalography (EEG) activity (Siegel, 2011). It was only recently recognized that aperiodic activity contains rich information about the current brain state (He et al., 2010; Lendner et al., 2020) and reliably discriminates wakefulness and REM sleep (Lendner et al., 2020; Kozhemiako et al., 2022). Aperiodic activity can be approximated by a 1/f^X relationship (Miller et al., 2009), where the spectral slope, specifying the "steepness" of the 1/fx power spectrum, ranges from -2 to -4 (Colombo et al., 2019; Lendner et al., 2020). In some instances, the slope might systematically change after a "bend" in the power spectrum, also referred to as a spectral knee (Miller et al., 2009; Gao et al., 2020). To date, multiple approaches to estimate aperiodic activity have been introduced (Gerster et al., 2022). Popular tools model aperiodic activity by either a first-degree polynomial or one or two Lorentzian functions (Miller et al., 2009; Gao et al., 2017; Donoghue et al., 2020), which can include the estimation of a spectral knee. Recent findings showed that this spectral knee corresponds to a time constant, which is also referred to as an intrinsic neural timescale (Murray et al., 2014; Gao et al., 2020). Here, we employ the term spectral knee and intrinsic neural timescale interchangeably to refer to the definition in the frequency or time domain.

Intrinsic neural timescales have been observed on various spatiotemporal scales (Soltani et al., 2021; Wolff et al., 2022). To date, there is no consensus on how timescales should be best approximated (Fig. 1), and their functional relevance for behavior and the current brain state is not very well understood. One explanation suggests that timescales reflect temporal integration windows over which behaviorally relevant information (such as working memory) can be integrated (Wasmuht et al., 2018; Soltani et al., 2021; Wolff et al., 2022). In line with this idea, timescales typically become longer in the higher-order association cortex compared with primary sensory cortices (Murray et al., 2014).

A major caveat when estimating aperiodic activity is that fitting in different frequency ranges yielded vastly different or even contradicting results depending on whether the fit included lower (e.g., 1-50 Hz) or higher frequencies (e.g., 30-50 Hz; Colombo et al., 2019; Miskovic et al., 2019; Lendner et al., 2020; Bódizs et al., 2021). To date, it remains unknown why the \sim 30-50 Hz range [initially proposed by Gao et al. (2017)] is particularly well suited to discriminate different brain states. The observed frequency dependence could potentially be attributed to the fact that the electrophysiological power spectrum cannot be adequately approximated by a single 1/f relationship. Instead, it appears to be governed by multiple distinct power lawlike relationships, which are systematically separated by several spectral knees. In line with this consideration, Miller et al. (2009) reported that the power spectrum exhibited multiple spectral knees. Specifically, they reported a knee at \sim 75 Hz where the slope changed from -2.5 to -4. Therefore, it is plausible to consider that additional timescales may represent an organizing principle that varies according to the brain state.

Here, we investigate how the precise fitting range of aperiodic activity relates to the current brain state. We introduce a principled approach on how aperiodic activity can be estimated when the number of spectral knees is unknown. We then demonstrate that aperiodic activity is shaped by multiple spectral knees (reflecting intrinsic neural timescales) that are either state-invariant or state-dependent.

Materials and Methods

Participants

Study 1. We obtained intracranial recordings from 15 pharmacoresistant epilepsy patients $(35.0\pm11.1~{\rm years};~{\rm mean}\pm{\rm SD};~{\rm nine}~{\rm females})$ who underwent presurgical monitoring with implanted depth electrodes (Ad-Tech Medical Instrument), which were placed stereotactically to localize the seizure onset zone. All patients were recruited from the University of California Irvine Medical Center. Electrode placement was exclusively dictated by clinical considerations, and all patients provided written informed consent to participate in the study. Participant selection was based on magnet resonance imaging (MRI) confirmed electrode placement in the medial temporal lobe (MTL) and prefrontal

cortex (PFC). We only included patients where one seizure-free night was available. The study was not preregistered. All procedures were approved by the Institutional Review Board (IRB) at the University of California (protocol number, 2014-1522) and conducted in accordance with the sixth Declaration of Helsinki. This dataset was also included in a subset of the analyses reported in Lendner et al. (2023).

 $Study\,2.$ The dataset included intracranial recordings from 20 pharmacoresistant epilepsy patients $(30.7\pm9.4~\rm years;~\rm mean\pm\,SD;~11~\rm female)$ who had subdural electrode arrays placed on the brain surface of the lateral frontal, temporal, and parietal cortical areas for the localization of seizure foci. These arrays were composed of circular platinum electrodes with 2.3 mm diameter exposed, at 1 cm interelectrode distance (center-to- center). All patients participated in a purely voluntary manner, after providing informed written consent, under experimental protocols approved by the IRB of the University of Washington (12193). All patient data were anonymized according to IRB protocol, in accordance with Health Insurance Portability and Accountability Act mandate. These data originally appeared in the manuscript "Power-Law Scaling in the Brain Surface Electric Potential" published in PLoS Computational Biology in 2009 (Miller et al., 2009) and made publicly available here (Miller, 2019).

 $Study\,3.$ Twelve patients with intractable epilepsy participated in this study $(26.6\pm13.2~{\rm years};~{\rm mean}\pm{\rm SD};~{\rm three}~{\rm females}),$ which were also included in Lendner et al. (2020). Data were collected during the explantation of the intracranial electrodes from induction of anesthesia up to the point of their removal. All patients received total intravenous anesthesia with propofol and remifentanil at the University Hospital of Oslo. All patients were placed back on their usual antiepileptic medication before the procedure. All participants or their parents provided informed written consent according to the local ethics committee guidelines (Regional Committees for Medical and Health Research Ethics in Oslo case number 2012/2015; extension 2012/2015–8) and the sixth Declaration of Helsinki.

Experimental design and procedures

Study 1: sleep monitoring. We recorded a full night of sleep for every participant. Recordings typically started ~8:00-10:00 P.M. and lasted for ~10-12 h. Only nights that were seizure-free were included in the analysis. Polysomnography was collected continuously. We recorded from all available intracranial electrodes. In order to facilitate sleep staging based on established polysomnography criteria, we also recorded scalp EEG, which typically included recordings from electrodes Fz, Cz, C3, C4, and Oz according to the international 10-20 system. Electrooculogram (EOG) was recorded from four electrodes, which were placed around the right and left outer canthi. All available artifact-free scalp electrodes were low-pass filtered at 50 Hz, demeaned and detrended, downsampled, and referenced against the average of all clean scalp electrodes. EOGs were typically bipolar referenced to obtain one signal per eye. A surrogate electromyogram signal was derived from electrodes in immediate proximity to the neck or skeletal muscles, by high-pass filtering either the electrocardiogram or EEG channels above 40 Hz. Sleep staging was carried out according to Rechtschaffen and Kales guidelines by trained personnel in 30 s segments (Rechtschaffen and Kales, 1968).

Study 2: fixation. Participants were asked to keep their eyes open and maintain fixation on an "X" on the wall 3 m away, for several minutes $(179 \pm 27 \text{ s}, \text{ mean} \pm \text{SEM})$. They were instructed to remain motionless and keep their eyes open, blinking if they needed to.

Study 3: anesthetic management. Data were collected in the operating room during the explantation of the intracranial electrodes from induction of anesthesia up to the point of their removal. The awake state was defined as time before start of propofol; anesthesia was defined as the time after loss of consciousness (unresponsiveness to verbal commands assessed by study personnel and attending anesthesiologist). All patients received a premedication with 3.75–7.5 mg midazolam (Dormicum). Propofol (Propolipid, Fresenius Kabi) and remifentanil (Ultiva, GlaxoSmithKline) were administered by computer-controlled infusion pumps (B Braun Perfusor Space) using a target-controlled infusion

program (Schnider for propofol and Minto for remifentanil) in order to achieve plasma concentrations sufficient for anesthesia and analgesia. Prior to start of anesthesia, all patients received an infusion of Ringer's acetate (5 ml/kg) to prevent hypotension during anesthesia induction, as well as 3–5 ml 1% lidocaine intravenously to prevent pain during propofol injection. All patients were preoxygenated with 100% oxygen and received the nondepolarizing muscle-relaxant cisatracurium for intubation (Nimbex, GlaxoSmithKline). After intubation, the inspiratory oxygen fraction was reduced to 40%.

Intracranial EEG data acquisition

All electrophysiological data in Study 1 was acquired using a 256-channel Nihon Kohden recording system (model JE120A), analog filtered at 0.01 Hz, and digitally sampled at 5,000 Hz. Study 2 recorded at the bed-side with Neuroscan Synamps 2 amplifiers (Compumedics Neuroscan), in parallel with a clinical recording system (XLTEK or Nicolet-BMSI). The signal was digitally sampled at 10,000 Hz (Subjects 1–4; subsequently downsampled to 1,000 Hz) or 1,000 Hz (Subjects 5–20). Data in Study 3 were recorded on a Natus NicoletOne system with a 128-channel capacity and a digitization rate of 1,024 Hz for up to 64 or 512 Hz for up to 128 channels.

Image data acquisition and electrode reconstruction

Electrode reconstruction was typically performed based on anonymized postoperative computer tomography scans and presurgical MRI scans, which were routinely acquired during clinical care. MRI scans were typically 1 mm isotropic. For Studies 1/3, we employed the approach outlined by Stolk et al. (2018). The details regarding electrode reconstruction for Study 2, including brain shift correction following the craniotomy, can be found in detail here (Miller, 2019). In all instances, electrodes were warped onto the Montreal Neurological Institute template brain to facilitate visualization in a common space.

Quantification and data analysis

Preprocessing. Study 1. In every subject, we selected all artifact-free available electrodes in the MTL (N=150) and PFC (N=348), which were then demeaned, detrended, notch-filtered at 60 Hz and its harmonics, bipolar referenced to its immediate lateral neighboring electrode, and finally downsampled to 500 Hz. Then all resulting traces were manually inspected, and noisy, epileptic, and artifact-contaminated channels were excluded. Data were epoched into 30-s-long, nonoverlapping segments according to the hypnogram.

Study 2. All available, artifact-free electrodes (N=1,142) that were included in the publicly available dataset were included in the study. Data were re-referenced to bipolar pairs (nearest neighbors; N=1,973), demeaned, detrended, and notch-filtered at 60 Hz and its harmonics. Given that these recordings were relatively short, we epoched the recordings into 4-s-long segments with 75% overlap.

 $Study\ 3$. All artifact-free available neocortical electrodes were included ($N\!=\!632$). We did not include electrodes in the archicortex, given that MTL electrode placement was inconsistent at the group level and precluded subsequent group analyses. Data were demeaned; detrended; notch-filtered at 50 Hz and its harmonics; if necessary, bipolar referenced to its immediate lateral neighboring electrode; and downsampled to 512 Hz (for subjects that were sampled at 1,024 Hz). Data were epoched into 10-s-long segments.

Spectral analysis. Spectral estimates were calculated by means of multitaper spectral analyses as implemented in FieldTrip (Oostenveld et al., 2011) based on discrete prolate spheroidal sequences in up to 143 logarithmically spaced bins between 0.25 and 181 Hz, depending on the available trial length. We adjusted the temporal and spectral smoothing to approximately match a ± 2 Hz frequency smoothing. Notch-filtered frequencies were interpolated. Spectral estimates across several channels within a region were either averaged or approximated by the first principal component, which yielded equivalent results. Aperiodic estimates were then extracted for every channel as outlined below.

Estimation of aperiodic activity. Aperiodic activity was estimated from three complementary approaches (compare Fig. 1), polynomial

fitting, FOOOF fitting and iterative fitting. We did not consider alternative approaches, such as IRASA (Wen and Liu, 2016), given the potential sensitivity to noise characteristics and aliasing (Chaoul and Siegel, 2021), which might bias the detection of additional high-frequency knees.

Polynomial fitting: To estimate the spectral slope in different frequency bands, we utilized first-degree polynomial (linear) fitting in log–log space, thus yielding an instantaneous spectral exponent (slope, χ) and offset (y-axis intercept, c), for a given fitting range. EEG spectra were fitted using variable endpoints (from a fixed starting point at 0.5 Hz up to 128 Hz, 17 logarithmically spaced bins), variable starting points (from 0.5 Hz to a fixed endpoint at 128 Hz, 17 logarithmically spaced bins), and a fixed bandwidth with varying center frequencies [0.5 to 128 Hz; ±1 octave (oct.); 17 logarithmically spaced bins] or in comparable ranges (e.g., 30–50 Hz; e.g., for illustration in Fig. 1Ciii) based on previous reports (Gao et al., 2017; Lendner et al., 2020).

FOOOF fitting: In order to obtain estimates of aperiodic activity, we employed the FOOOF algorithm (Donoghue et al., 2020). EEG spectra were fitted in variables ranges, e.g., linearly spaced from 1 to 100 Hz. Aperiodic activity was defined by its slope parameter χ , the y-intercept c, and a constant k (reflecting the knee parameter) as follows (Eq. 1):

aperiodic fit =
$$10^{c} * \frac{1}{(k + f^{\chi})}$$
. (1)

The relationship of the knee parameter k and the knee frequency f_k is given by the following (Eq. 2):

$$f_k = \mathbf{k}^{\frac{1}{\chi}}.\tag{2}$$

The timescale in the frequency domain can be calculated from the knee frequency f_k as follows (Eq. 3):

$$\tau = \frac{1}{2 * \pi * f_k}.\tag{3}$$

Numerical approximation by iterative fitting: While a linear fit does not assume any spectral knees, the FOOOF algorithm models the knee parameter as a Lorentzian function with one spectral knee. In order to model aperiodic activity with multiple knees and without the need to predefine the number of expected spectral knees, we implemented an iterative fitting procedure (outlined in Fig. 3B). We employed logarithmically scaled, multitapered power spectra with >>100 bins to obtain reliable estimates for the subsequent analyses. To attenuate the effect of oscillatory peaks, we first smoothed the spectrogram with a pseudo-Gaussian (three passes of a sliding average). Smoothing left the 1/f structure unchanged, while it markedly reduced oscillatory activity (Fig. 3Bi). In order to account for the impact of residual oscillatory peaks after smoothing, we rejected identified points as outlined below that were in close proximity ($\pm 1/4$ oct.; compare Fig. 3Biv). Next, we locally fit the spectrum within first-degree polynomials between the boundaries defined by f_1 and f_2 , thus yielding N (number of predefined center bins) local fits with y-intercept c and slope parameter χ (Fig. 3Bii). We then identified frequencies where the aperiodic activity did not change and was similar to the aperiodic activity at neighboring frequencies, thus defining a minimal basis set of aperiodic parameters that captured the power spectrum. Note that this approach does not identify oscillations, which are characterized by a peak in the spectrum (rapid rise and decay within a few Hertz), thus biasing linear fits. Algorithmically, this was achieved by assessing the parameters c and χ , which defined a set of spectral states in a 2D space across all N linear fits (Fig. 3Biii). This 2D representation was then visualized as a corresponding spectral trajectory, which was defined as the Euclidean distance between neighboring points $p_{c,\chi}$ and $p_{c+1,\chi+1}$. We then defined locally stable spectral estimates as the local minima (peak detection on the inverted signal) of the spectral trajectory (Fig. 3Biv), thus identifying frequencies where parameters c and χ remained stable. Sequential basins that occurred within a narrow frequency band (±1/4 oct.; gray-shaded box in Fig. 3Biv) were excluded to further discount the influence of oscillatory activity. Next, we medianaveraged all estimates for c and χ within a window w (e.g., $\pm 1/2$ oct.; fit bandwidth) to obtain the minimal basis set of parameters that defined the aperiodic activity. Then we evaluated the polynomial for the averaged parameters at all local minima (Fig. 3Bv), yielding a set of local fits. Finally, we defined the spectral knees as the intersections of the different fitted lines (projected to the nearest point on the smoothed spectrum; Fig. 3Bv,vi). Lastly, we merged adjacent detections that had the same slope parameter χ or were smaller than w. All spectra were initially fitted with the following parameters: $f_1 = 1$ Hz; $f_2 = 150$ Hz; smoothing factor = 1/2 oct.; and fit bandwidth = $\pm 1/2$ oct. In the case that parameters did not converge, the smoothing factor and fit bandwidth were lowered to match, e.g., a third or quarter oct.

Estimating the timescale from the autocorrelation function in the time domain: For illustration purposes, we employed three complementary approaches to extract the timescale τ from the autocorrelation function (Murray et al., 2014; Raut et al., 2020; Wolff et al., 2022). The autocorrelation function was fitted with an exponential function (Eq. 4), where A reflected the amplitude, B the offset, Δt the time lag, and τ the timescale as follows:

expontential fit =
$$A * \left[\exp \frac{-\Delta t}{\tau} + B \right]$$
. (4)

Alternatively, the temporal delay τ was defined as the time it took for the signal to decay by 50%. Lastly, we fitted the autocorrelation with a half-Gaussian (alternatively, spline fits have been employed; Raut et al., 2020) and defined the timescale τ as the full-width at half-maximum (FWHM) of the fitted curve.

Simulation of aperiodic activity and validation

We simulated EEG power spectra with two spectral knees to validate the iterative fitting procedure. The EEG power spectrum was modeled as the product of two Lorentzian functions and a noise term (Eq. 5). The frequencies f were logarithmically spaced between 0.5 and 256 Hz with a lower slope parameter $\chi_{\rm L}$ that was half of the upper slope $\chi_{\rm H}$ (e.g., 3 and 6), the offset c was set to 2, and the knee parameter k defined the lower knee (see Equation 2; range = 20–3000; corresponding to \sim 2.5–14.5 Hz), while $f_{\rm h}$ defined the upper knee frequency (range 50–100 Hz). The noise term ε was scaled by a 1/f factor. To account for the difference in noise in simulations as compared with empirical recordings, the smoothing factor and bandwidth were lowered to match, e.g., a third or quarter oct. as outlined above as follows:

$$PSD = \frac{10^c * \frac{1}{(k + f^{\chi_L})}}{1 + \left(\frac{f}{f_h}\right)^{\chi_H}} + \frac{1}{f} \varepsilon.$$
 (5)

Across all iterations, the different parameter combinations, and noise levels, we modeled >400.000 spectra. The observed parameters for the low and high spectral knees were then correlated (Spearman rank correlation) against the ground truth model parameters. Across 1,000 iterations, we also obtained a surrogate distribution by shuffling the observed estimates 200 times. The observed correlation coefficients were then z-scored relative to surrogate distribution.

Statistical analysis

Unless stated otherwise, we employed two-tailed paired t tests and repeated-measure analysis of variance. We used FDR correction (Fig. 2C) or cluster-based permutation tests to correct for multiple comparisons as implemented in FieldTrip (Monte Carlo method; 1,000 iterations) based on either paired t tests or F tests. Clusters were formed across frequencies (e.g., Figs. 2B, 3I,I) by thresholding the statistical tests at p < 0.05. A permutation distribution was then created by randomly shuffling condition labels. Correlations with the hypnogram were assessed by means of Spearman rank correlations analogous to Lendner et al. (2020), where wake corresponded to 0, NREM sleep to 1–4, and REM to 5. Correlation values were transformed into z-scores as outlined below. Where applicable, we also employed random block swapping to obtain a surrogate distribution. The permutation p value

was obtained by comparing the cluster statistic to the random permutation distribution. The clusters were considered significant at p < 0.05 (two-sided for t tests, one-sided for F tests). In addition, we used binomial tests to infer if the observed number of outcomes across all observations was significant (e.g., the presence of spectral knee in Figs. 4E, 5E; yes/no probability, 0.5). In one instance (Fig. 2C), p values across several tests were combined by turning each p value into a z-score using the inverse normal cumulative distribution function. The resulting z-scores were then combined. The resulting combined p values were then obtained from the normal cumulative distribution function (Stouffer et al., 1949).

Moreover, we employed linear correlations (e.g., Figs. 1D, 2E). Correlation values were transformed into t values using the following formula (Eq. 6):

$$t = \frac{r * \sqrt{N-2}}{\sqrt{1-r^2}}. (6)$$

T values were then transformed into z values as deviations from the standard normal (Gaussian) distribution with the lower tail probability equal to the t statistics with the given degrees of freedom (Fig. 2B). Z values were considered significant at $z=\pm 1.96$, corresponding to an uncorrected two-tailed p value of 0.05. Effect sizes were quantified by means of Cohen's d (t tests) or eta squared (F tests). To obtain effect sizes for cluster tests, we calculated the effect size separately for all frequencies and averaged across all data points in the cluster.

Results

To test if aperiodic temporal regularities govern distinct brain states during sleep, we recorded whole-night intracranial EEG (iEEG) from 15 pharmacoresistant epilepsy patients who underwent presurgical evaluation (Fig. 1A) with electrodes implanted in the MTL (N = 150) and PFC (N = 348). Notably, grand-average power spectra exhibited prominent region-specific differences across the different sleep stages (Fig. 1B). Visually, these spectra exhibited multiple distinct oscillatory peaks and spectral knees that separated frequency ranges where the spectral slope exhibited a characteristic 1/frequency decay function (Fig. 1C). Depending on the precise fit range, positive, negative, or no associations can be observed (Fig. 1D). For example, the spectral slope at 2 Hz (±1 oct.) correlated positively with the hypnogram (Spearman rho = 0.55; single-subject MTL example; group-level results are reported in Fig. 2), while no association was observed at 16 Hz (rho = 0.01). For higher frequencies, negative correlations were evident (e.g., in the previously employed \sim 30–50 Hz band: rho = -0.54). These findings are strongly indicative of several independent processes that jointly shape the electrophysiological power spectra during different brain states. Given the prominent spectral slope differences in the various frequency bands in this example (0.5-1 Hz slope, -0.07; 20-45 Hz slope,-2.65; 64–128 Hz slope, -3.85), we reasoned that the transition points between the different frequency segments might be the result of characteristic spectral knees of the power spectrum, which correspond to intrinsic neural timescales (see Fig. 1E,F for estimation in the time and frequency domain). In the time domain, timescales are typically extracted from the autocorrelation function by fitting an exponential, spline, or Gaussian function or by estimating the decay time that is necessary for a reduction by a predefined factor (e.g., 0.5; see Materials and Methods; Fig. 1E). In the frequency domain, the intuitive approach is to quantify the spectral knee, which can be approximated by, e.g., the peak of the first differential of the spectrum or by a Lorentzian fit (Fig. 1F). The time constant of the Lorentzian function directly corresponds to the constant of the exponential

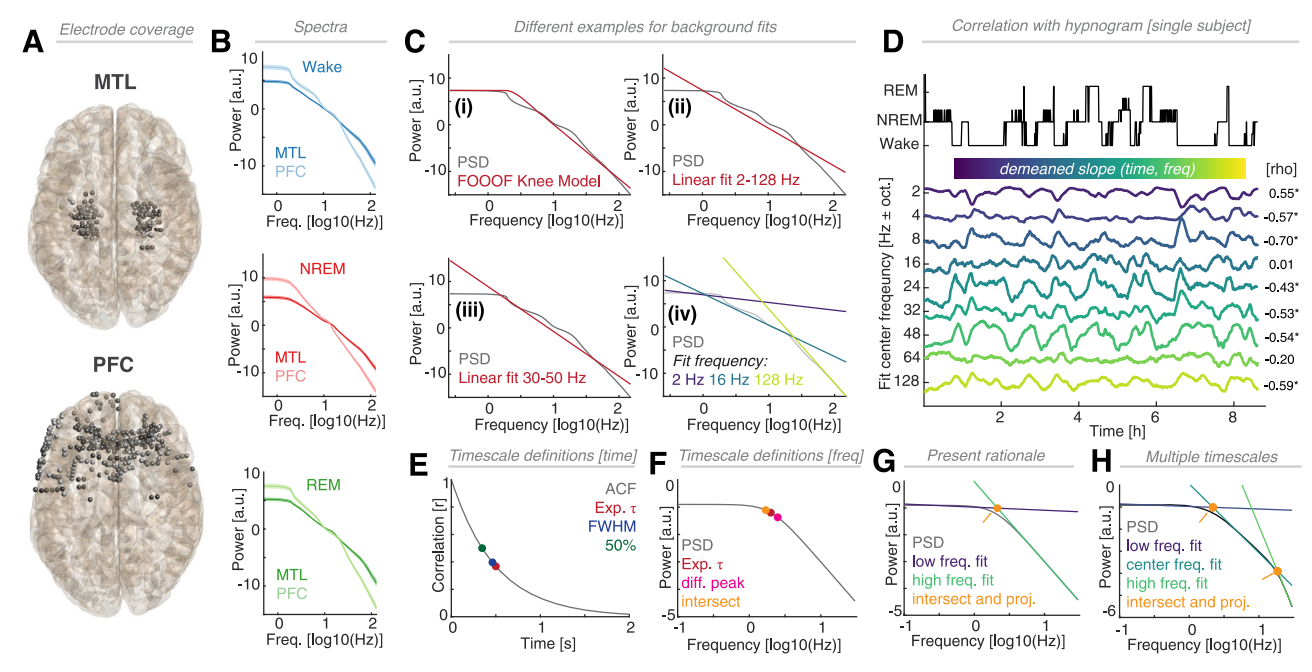


Figure 1. Nonuniform distribution of electrophysiological aperiodic activity during sleep. *A*, Intracranial electrode placement (*N* = 15 subjects; 498 bipolar electrode pairs) in the MTL (*N* = 150; top panel) and PFC (*N* = 348; bottom panel). *B*, Grand-average power spectral densities (PSD) for the MTL (dark shading) and PFC (light shading) in the wake state (blue; top panel), NREM (red; center) and REM sleep (green; bottom panel). Note the overall flatter PSD slope on the MTL across different states as well as the presence of multiple bends at various frequencies. *C*, Approximation of aperiodic activity (dark red) of the PSD (black; example spectrum from the MTL). *i*, F000F fit of a Lorentzian function with a time constant (knee parameter). *ii*, Linear fit across the PSD from 2 to 128 Hz. *iii*, Linear fit from 30 to 50 Hz. *iv*, Linear fit with varying center frequencies (±1 oct.); three example fits (center, 2, 16, and 128 Hz) are shown. *D*, Correlation of the hypnogram (top trace) and smoothed linear slope fits (demeaned estimates; colored traces) at various center frequencies (from 2 to 128 Hz; MTL, single-subject example; for group data, see Fig. 2*B*). The same color conventions as in panel *C*, *iv*. Note that most fits are significantly correlated (note, the sign flip) with the hypnogram (right; Spearman rho; *p < 0.05 as obtained from a surrogate distribution; 1,000 iterations; random block swapping procedure). *E*, Illustration of different approaches to estimate intrinsic timescales in the time domain. Note, in neural systems, the ground truth is typically unknown. The timescale of the autocorrelation function (ACF; exponential decay; black) can be quantified as the time constant τ (red). Alternative approaches for timescale estimation include the time lag at FWHM (assuming a spline or Gaussian fit to the ACF; blue) or a signal reduction by 50% (*r* = 0.5; green). *F*, Estimation of intrinsic timescales in the frequency domain. The characteristic spectral knee of the PSD (gray) reflects th

decay function per the Wiener-Khinchin theorem (Gao et al., 2020). Critically, while previous work indicated the presence of only one or two spectral knees, the correlation analysis of frequency- (±1 oct.) and time-resolved slope estimates (entire night; 30 s segments) with the hypnogram (compare Fig. 1D) is indicative of multiple bends in the power spectrum (spectral knees) that cannot be estimated using conventional methods. Here, we outline how iterative spectral fitting can be employed to numerically approximate the spectrum with multiple spectral knees, without the need to predefine the number of expected knees. This was achieved by estimating spectral segments where the power spectrum followed a distinct 1/f distribution. The spectral knee was then defined as the projection of the crossover point of two linear fits to the nearest point on the spectrum (Fig. 1G; outlined and validated in detail in Fig. 3). This approach enables capturing two or more spectral knees, which are indicating multiple, simultaneously present timescales (Fig. 1H).

Neural aperiodic activity is region- and state-specific

To demonstrate the presence of multiple, brain state-dependent spectral knees, we first employed first-degree polynomial (linear) fitting with multiple different fit characteristics (Fig. 2A). All power spectra were fit using a variety of parameters, either keeping the starting point constant (variable endpoints), parametrically varying the starting point (keeping the endpoint

constant), or fitting different center frequencies (in a one oct.wide band). This analysis was conducted separately for MTL and PFC in 30 s segments as defined by the hypnogram. The time-resolved (across the night) slope estimates in the various frequency bands were then correlated with the hypnogram (analogous to Fig. 1D; Spearman rank correlation; sleep stages were ranked as wake, NREM1-4, REM). Correlation coefficients were standardized by z-transformation (see Materials and Methods) and compared by means of cluster-based permutation testing. For the different fitting approaches, we observed several significant clusters (Fig. 2B; cluster permutation tests based on paired t tests) that spanned multiple frequency bands (variable end, Pos. Cluster 1 from 6 to 32 Hz, p = 0.010; d = 0.68; Pos. Cluster 2 from 0.5 to 1 Hz, p = 0.021; d = 0.84; variable start, Neg. Cluster 1 from 16 to 45 Hz, p < 0.001; d = -1.03; different center frequencies, Pos. Cluster 1 from 11 to 16 Hz, p = 0.010; d = 0.96; Pos. Cluster 2 from 0.5 to 0.7 Hz, p = 0.013; d = 0.81; Neg. Cluster 1 from 23 to 45 Hz, p < 0.001; d = -1.05). Hence, we combined and FDR-corrected the p values across the three different approaches (Fig. 2C; Stouffer method; see Materials and Methods). This analysis demonstrated that the spectral slope in the frequency range ~20-45 Hz, and not across the entire spectrum as expected from $1/f^{\chi}$ process with one decay constant, dissociated how MTL and PFC dynamics aligned with the hypnogram (Fig. 2D). This effect is further illustrated in Figure 2E

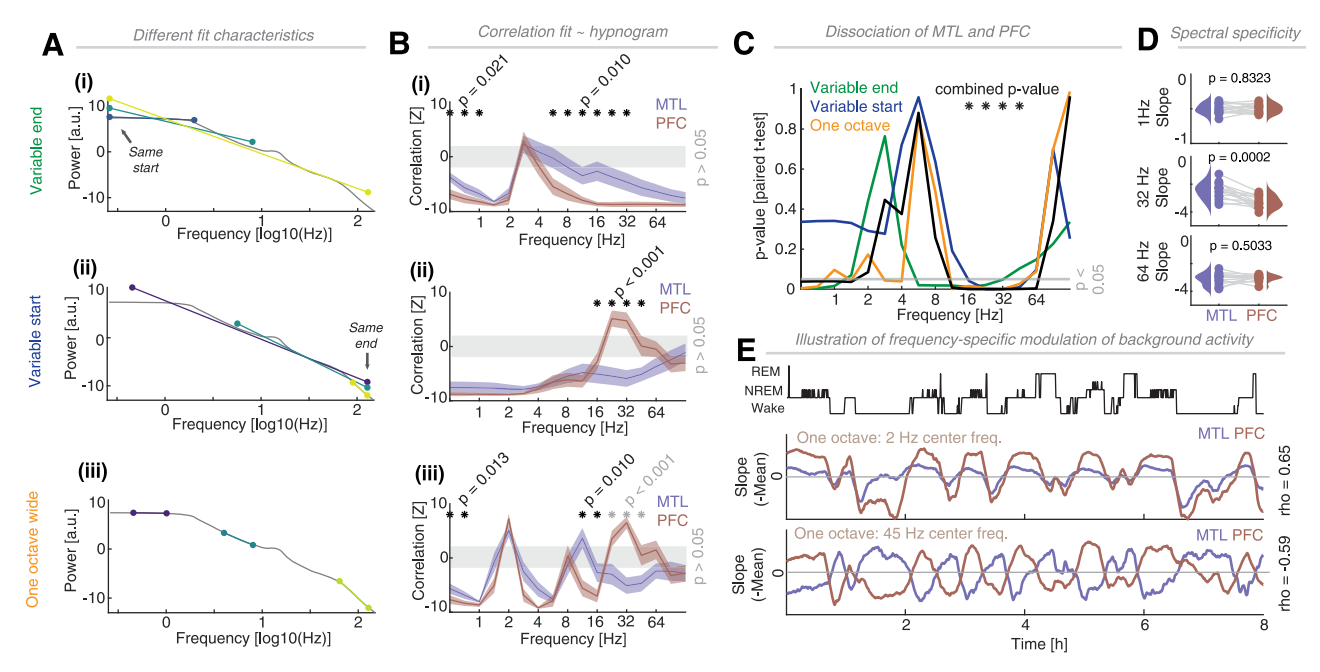


Figure 2. State-dependent aperiodic activity is region- and frequency-specific. **A**, Illustration of different linear fit ranges. **i**, Fit from a fixed 0.25 Hz starting point to variable endpoints. **ii**, Fit from variable starting points to a fixed endpoint of 128 Hz. **iii**, Fit at variable center frequencies (±1 oct.). **B**, **i**, Correlation (*z*-scored; mean ± SEM; N = 15) between the individual hypnograms and spectral slopes (linear fits with variable ends) for the MTL (dark blue) and PFC (dark red). The gray-shaded area depicts the range of $z = \pm 1.96$ (corresponding to an uncorrected, two-tailed p > 0.05). Asterisks indicate the significant difference between the correlations in the MTL and PFC. Note that both correlations show a similar trend and that correlations remain nonsignificant for endpoints at ~4 Hz. **ii**, Correlation between the hypnograms and spectral slope (linear fits with variable starting points; the same conventions as in the top panel). We observed a significant difference between MTL and PFC correlation in the range from 16 to 45 Hz. Note that the PFC correlations in this frequency range exhibit a sign reversal, which indicate the presence of two spectral features (at ~20 and ~64 Hz) that are specific to the PFC. **iii**, Correlation between the hypnograms and spectral slope (linear fits with varying center frequencies; the same conventions as in the top panel). Note that correlations exhibit multiple sign reversals, which are similar between the MTL and PFC (e.g., at ~2 Hz) with the exception of a prominent dissociation in the range from 23 to 45 Hz. **C**, Summary statistics across the observations in panel **B**. Uncorrected *p* values as a function of frequency for the comparison between MTL and PFC correlations to the hypnogram (variable end in green; variable start in dark blue; different center bin in orange; the gray line depicts the p < 0.05 threshold). p < 0.05 threshold). p < 0.05 threshold). p < 0.05 threshold) in the range from 16 to 45 Hz. **D**, Comparison of the s

(single-subject example) highlighting aligned spectral slopes (demeaned for illustration purposes) for a 2 Hz center frequency bin, while the slope at 45 Hz exhibited a striking antiphasic pattern. Collectively, this set of findings demonstrated that aperiodic activity as quantified by the spectral slope systematically varies as a function of frequency. As a control analysis, we altered the numerical encoding of the hypnogram (wake—REM—N1-4), which yielded comparable results (variable end, Pos. Cluster 1 from 4 to 45 Hz, p < 0.001; d = 0.94; Pos. Cluster 2 from 0.5 to 2 Hz, p = 0.003; d = 1.05; variable start, Neg. Cluster 1 from 22 to 45 Hz, p < 0.001; d = -1.45; different center frequencies, Pos. Cluster 1 from 0.5 to 1.4 Hz, p < 0.001; d = 1.17; Pos. Cluster 2 from 11 to 16 Hz, p = 0.016; d = 0.98; Pos. Cluster 3 from 3 to 4 Hz, p = 0.030; d = 0.81; Neg. Cluster 1 from 23 to 45 Hz, p <0.001; d = -1.36; combined p < 0.05 in the range from 16 to 64 Hz). This observation then raises the question why only certain frequency bands correlated with the hypnogram. One possibility was that the dissociation between MTL and PFC in a narrow frequency range was the result of two additional spectral knees at \sim 16-23 and \sim 45 Hz.

Multiple spectral knees shape 1/f activity

Next, we addressed the question if the differences in spectral slope between brain states could be the result of additional, previously unidentified spectral knees in the \sim 20–45 Hz frequency

range. Since typical approaches only estimate one or two spectral knees (Fig. 3A), we devised an iterative fitting procedure that did not predefine the number of expected knees (Fig. 3B; see Materials and Methods). In brief, we iteratively fitted the spectrum in many possible frequency bands and identified the ranges where the spectral slope remained constant (corresponding to the basins in Fig. 3B). Spectral knees were then defined as the intersection of linear fits of two adjacent frequency segments (in which the spectral slope remained constant), i.e., identifying the frequency where the slope changed. Oscillations (as indicated by distinct peaks arising over the 1/f decay function) were attenuated by smoothing the power spectrum (leaving the 1/f function intact) and excluding multiple sequential basins (within ± 1/4 oct.). This approach yielded a set of fits and spectral knees (Fig. 3Bvi). To validate this approach, we simulated power spectra (modeled as two Lorentzian functions; see Materials and Methods) with varying parameters for upper and lower spectral knees in presence of 1/f noise (Fig. 3C). The simulated spectra were then iteratively fitted, and the observed knee frequencies were correlated against the model knee frequencies (as ground truth; Fig. 3D). The observed correlations were z-scored relative to a surrogate distribution. We observed that both low- and highfrequency knees can be reliably recovered (Fig. 3E; low-frequency knee, average z = 11.35; p < 0.0001; high-frequency knee, average z = 4.93; p = 0.0050). Given the different spectral knee definitions

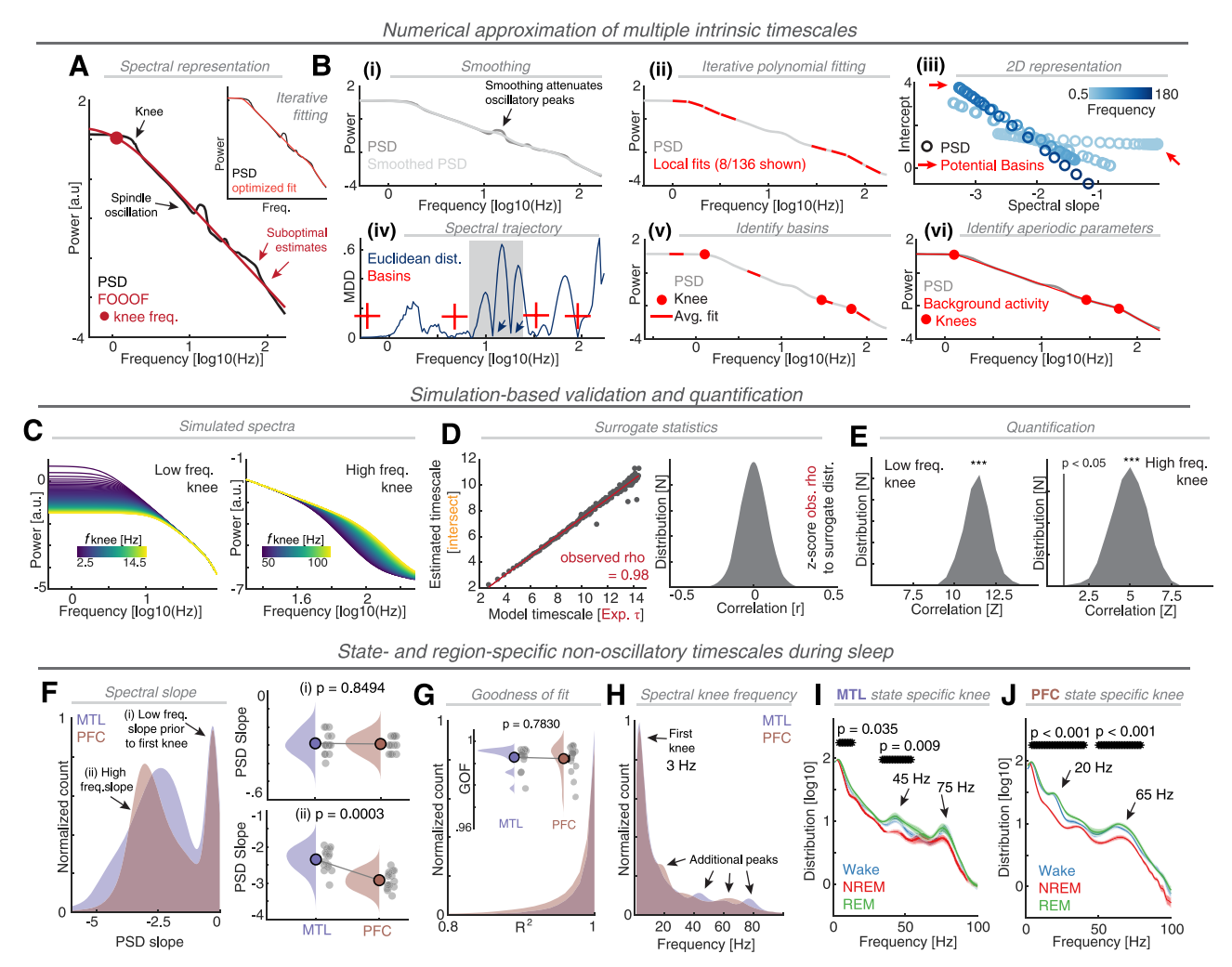


Figure 3. Numerical approximation of intrinsic timescales in the frequency domain. A, An exemplary power spectrum (PSD) and the respective Lorentzian fit (red; F000F model; with knee frequency highlighted as the red dot) indicate the presence of a low-frequency spectral knee (arrow) as well as discrete peaks (e.g., spindle oscillations at ~14 Hz). Overall, the power spectrum is well approximated by the aperiodic estimate (red), but clear deviations are evident, in particular for higher frequencies (red arrows), which might be indicative of additional spectral knees. The inset depicts the current approach to iteratively fit the spectrum to obtain a set of parameters (optimized fit in light red). B, Numerical approximation of different spectral knees with iterative spectral fitting: (\hat{j}) spectral smoothing attenuates oscillatory peaks (arrow) but leaves the $1/f^{x}$ decay function constant. Note that this step does not fully remove all oscillatory bumps, hence requiring an additional subsequent selection step (compare panel iv). ii, The aperiodic activity is then linearly fitted for every frequency segment (loq-log scale) by a first-degree polynomial using a one oct.-wide frequency band (in red; 8 exemplary fits out of 136 are shown). iii, Representation of the fit estimates in a 2D coordinate system (slope and intercept), color-coded by the center frequency of the respective bin (in blue; from 0.5 to 180 Hz). Red arrows indicate two (out of multiple) potential local minima where the fit parameters remain constant (termed basins and as algorithmically defined in iv). iv, Euclidean distance between adjacent data points (compare panel iii). Periods where spectral fits remain constant were identified as local minima close to zero (red crosses). Note that sequential basins that occurred within a narrow frequency band ($\pm 1/4$ oct.; blue arrows indicate rejected points within the gray-shaded box) were excluded. In this example, basins (blue arrows) between 10 and 30 Hz were excluded (gray-shaded box), since they reflected the spindle oscillation and its harmonic. v, The spectrum was then fitted using the parameters at the local minima across all available frequencies. Spectral knees were then identified as the intersects of two linear fits, projected onto the nearest point on the smoothed curve (as illustrated in Fig. 16). vi, Finally, the identified linear fits were linearly extended to span the entire range between obtained knee frequencies to define a reduced set of parameters, which best describe the power spectrum. C, Simulated PSDs (see Materials and Methods) with multiple spectral knees for lower (left) and higher frequencies (right). D, Numerical approximation of timescales. Left, Example of one iteration (out of 1,000), which examined each modeled low-frequency knee parameter once. Note, the timescale of simulated spectra was defined by parameter τ , while the knee was approximated by the intersect method (compare Fig. 1F). Overall, a high correlation (rho = 0.98) between simulations and estimates was observed. Right, Surrogate distributions. Observed correlations were then z-scored relative to the surrogate distribution (note the observed value is outside of the displayed rho = ± 0.5 range). $\textbf{\textit{E}}$, Distribution of z-scored correlations for the low-frequency (left) and high-frequency knees (right) reveals consistent z-scores >1.96 (two-tailed p < 0.05; *** $p \le 0.005$), hence indicating that spectral knees can be well approximated using iterative fitting. F, Left, Distribution of all observed spectral slopes estimates per region (MTL and PFC). Note, the bimodal distribution and the consistency for slope values close to 0, which reflect the spectrum prior to the first knee. Top right, Statistical comparison of the PSD slope prior to the first knee (dots depict individual participants). Bottom right, Statistical comparison of the PSD slope after the first knee reveals overall flatter slopes in the MTL than PFC (quantification of the effect in Fig. 1B). G, Goodness-of-fit of the power spectrum using the iterative fitting approach. The inset depicts individual average observations; no difference between MTL and PFC spectra was observed. H, Distribution of observed knee parameters. Additional peaks in the range >20 Hz indicate the presence of additional spectral knees. I, State-specific distribution (normalized density) of MTL spectral knees in log spacing reveals distinct peaks at ~45 and \sim 75 Hz. J, The same analysis for all PFC contacts indicates additional knees at \sim 20 and \sim 65 Hz.

in the model parameter and numerical approximation (as outlined in detail in Fig. 1E,F), the observed values were systematically lower than the model parameters (note, the offset is approximately constant across the logarithmically scaled

spectrum and corresponds to \sim 0.2 oct.). However, the highly significant correlations for lower and higher spectral knees (Fig. 1*E*) indicated that characteristic spectral knees were successfully approximated.

Subsequently, we iteratively fitted all power spectra during sleep. We observed that spectral slopes were generally flatter in the MTL than in the PFC (Fig. 3F) after the first knee $(t_{(14)} = 4.83; p = 0.0003; d = 1.25; MTL, -2.34 \pm 0.08; PFC,$ -2.92 ± 0.06 ; mean \pm SEM). Prior to the first knee, spectra in both regions were almost flat and did not differ $(t_{(14)} = 0.19;$ p = 0.8494; d = 0.05; MTL, -0.29 ± 0.02 ; PFC, -0.29 ± 0.01 ; mean ± SEM). Overall, goodness-of-fit (quantified by the explained variance R^2) were high (MTL, $R^2 = 0.995 \pm 0.001$; PFC, $R^2 = 0.995 \pm 0.002$; median \pm SEM) and did not differ between both regions ($t_{(14)} = 0.28$; p = 0.7830; d = 0.07). While the majority of spectra (across participants and electrodes) exhibited a low-frequency knee (~2-3 Hz; no differences between regions, $t_{(14)} = -1.72$; p = 0.1081; d = -0.44; MTL, 2.0 ± 0.4 Hz; PFC, 2.4 ± 0.7 Hz; mean \pm SD), we also observed additional spectral knees in various higher frequencies (Fig. 3H). On average, we observed three knees per region-of-interest (MTL, 3.0 ± 0.1 ; PFC, 3.0 ± 0.1 ; median \pm SEM; $t_{(14)} = 0.69$; p = 0.4985; d = 0.18). Specifically, additional spectral knees were observed at ~45 and \sim 75 Hz in the MTL (Fig. 3I) and at \sim 20 and \sim 65 Hz (Fig. 3J) in the PFC. Critically, these spectral knees were brain statedependent in the MTL (Cluster 1 from 34 to 54 Hz, p = 0.009; $\eta^2 = 0.20$; Cluster 2 from 4 to 13 Hz, p = 0.035; $\eta^2 = 0.28$; cluster permutation tests based on F tests) and PFC (Cluster 1 from 4 to 40 Hz, p < 0.001; $\eta^2 = 0.48$; Cluster 2 from 50 to 79 Hz, p < 0.001; $\eta^2 = 0.25$), hence dissociating different sleep states from wakefulness in both regions. Visually, the high-frequency peak in the MTL at ~75 Hz appears more prominent than the high-frequency PFC peak; however, it is critical to highlight that both only reflect peaks of the underlying distribution. Multiple scenarios are conceivable that might explain this apparent difference and include underlying anatomical or regionspecific biophysical differences, as well as true differences in knee variability or spatial sampling in different cortical areas.

In sum, the numerical approximation of spectral knees further supports the idea that the aperiodic power spectrum is not uniform but differs as a function of frequency and brain state. Critically, our iterative fitting approach recovers spectral knees at \sim 20 Hz (in the PFC) and \sim 45 Hz (in the MTL), which explains why the slope fits in the 20 to 45 Hz frequency range dissociates MTL and PFC brain state-dependent dynamics (compare Fig. 2C).

Multiple neural timescales govern different cortical states during sleep

Having validated our approach with simulated data, we next sought to recover spectral knees in empirical data. As a validation dataset, we obtained resting-state iEEG data recorded from subdural grid electrodes (electrocorticography) from 20 participants during central fixation (Fig. 4A). Previously, Miller and colleagues (Miller et al., 2009; Miller, 2019) employed this dataset to test if electrical brain activity follows a 1/f scaling law. They found that the spectral slope steepened from approximately -2.5 to -4 after a spectral knee at 77 ± 14 Hz (mean \pm SD; range ~40 to ~120 Hz), which implied the existence of an intrinsic timescale at ~2-4 ms. Critically, the authors did not assess any potentials "knees" below <20 Hz and did not analyze electrodes that exhibited a discernible oscillatory peak in the power spectrum. Here, we reanalyzed the dataset using iterative fitting. In line with our previous analyses, we observed that the spectrum was not well approximated by a Lorentzian function with one spectral knee (Fig. 4B). Iterative fitting demonstrated that the spectral slope was almost flat prior to a first knee at ~4 Hz $(-0.33 \pm 0.05; \text{ median} \pm \text{SEM})$ and in the range from -2 to -5for higher frequencies (Fig. 4C). Overall goodness-of-fit was high as to be expected from iterative fitting to facilitate detection of spectral knees (Fig. 4D; $R^2 = 0.986 \pm 0.001$; median \pm SEM), indicating that the aperiodic spectrum was successfully captured.

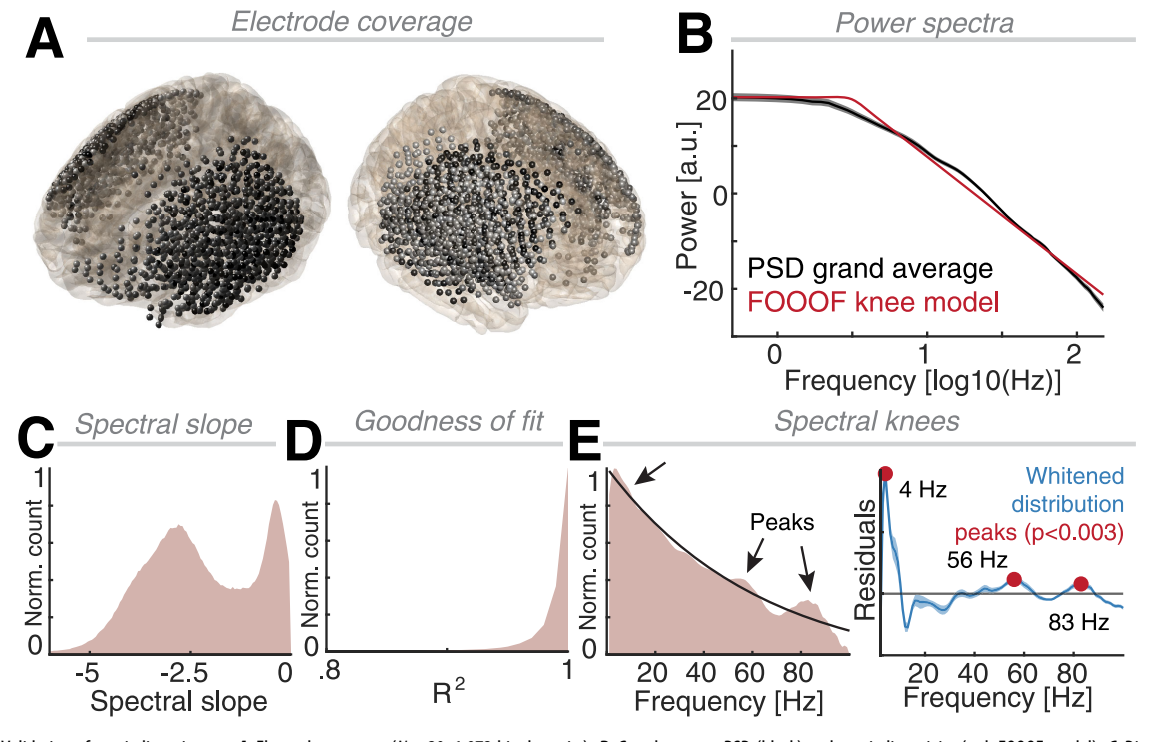


Figure 4. Validation of aperiodic estimates. **A**, Electrode coverage (N = 20; 1,973 bipolar pairs). **B**, Grand-average PSD (black) and aperiodic activity (red; F000F model). **C**, Distribution of all obtained PSD slopes analogous to Figure 3*F*. **D**, Overall goodness-of-fit was high ($R^2 > 0.99$). **E**, Left, Distribution of spectral knees. Right, At the group level, distinct peaks were evident at 4, 56, and 83 Hz (all p < 0.003, binomial tests) after subtraction of the exponential decay function to facilitate peak detection.

In addition to a low-frequency knee (at ~4 Hz; knee present in 18/20 participants; p = 0.0004; binomial test), we observed two additional knees (Fig. 4E) at \sim 56 Hz (p = 0.0026; 17/20 participants) and \sim 83 Hz (p = 0.0004; 18/20 participants) that were highly comparable with the estimates that were initially reported by Miller et al. $(77 \pm 14 \text{ Hz}; \text{ mean} \pm \text{SD}; 95\% \text{ CI}, 49-105 \text{ Hz}).$ Slight deviations can be accounted for by differences in spectral estimation (single taper with linear spacing in Miller et al., while multitapers with logarithmic spacing were employed here), the underlying fitting approach as well as inclusion of all available electrodes (without visually preselecting electrodes devoid of oscillations). Moreover, the identified peaks in Study 1 (\sim 65/75 Hz) were also within a similar range and were obtained from a similar patient group suffering from pharmacoresistant focal epilepsy. The slight differences with respect to the precise peak frequency might potentially be the result of different cognitive states (fixation vs spontaneous wakefulness before/after sleep) or electrode coverage (depth electrodes vs grid electrodes). In line with previous findings, the spectrum was steeper after the identified high-frequency knee at $\sim 80 \text{ Hz}$ ($t_{(19)} = 3.08$; p = 0.0061; d = 0.69; before knee, -2.71 ± 0.09 ; after knee, -3.50 ± 0.15 ; median \pm SEM). In sum, this set of findings further substantiates the idea that iterative fitting can recover spectral knees and replicates the presence of multiple characteristic timescales in human iEEG.

Propofol anesthesia dissociates state-invariant from state-dependent timescales

Lastly, we addressed the question whether the observed spectral knees are brain state-dependent or brain state-independent. If the spectral knees were independent of the underlying brain state, then the most parsimonious explanation for their presence would entail the presence of a characteristic timescale that indexes physiologic properties of underlying neuronal population, such as postsynaptic currents or conduction delays (Freeman and Zhai, 2009; He et al., 2010; Buzsáki et al., 2012). In contrast, brain state-dependent spectral knees might potentially imply second-order temporal organizing principles, such as network connectivity or temporal integration (Shinn et al., 2023).

To disentangle state-invariant from state-dependent neural timescales, we recorded iEEG in a separate sample of 12 participants during electrode explantation under general anesthesia with propofol (Fig. 5A). Recordings were obtained continuously in the operating room until the electrodes were physically removed, hence encompassing both wakefulness and general anesthesia. All participants received propofol as the anesthetic agent (see Materials and Methods for clinical management). In line with previous reports, we observed a strong modulation of the power spectrum during anesthesia (Fig. 5B). The spectral slope was steeper during anesthesia for both the slope in lower frequencies (before the first knee; $t_{(11)} = 7.68$; p < 0.0001; d = 2.22; wakefulness, -0.25 ± 0.03 ; anesthesia, -0.50 ± 0.03 ; median \pm SEM) and higher frequencies (after the first knee; $t_{(11)} = 3.74$; p = 0.0033; d = 1.08; wakefulness, -2.75 ± 0.16 ; anesthesia, -4.00 ± 0.26 ; median ± SEM; Fig. 5C). The overall goodness-of-fit was high and did not differ between both states (Fig. 5D, wakefulness, $R^2 = 0.978 \pm 0.003$; anesthesia, $R^2 = 0.973 \pm 0.003$; median \pm SEM; $t_{(11)} = 1.98$; p = 0.0729; d = 0.57). Critically, iterative fitting established the presence of spectral knees at ~5 Hz (wakefulness, in 12/12 participants; p = 0.0005; anesthesia, in 10/12 participants; p = 0.0386; binomial test) and ~75 Hz (wakefulness, in 12/12 participants; p = 0.0005; anesthesia, in 11/12 participants; p = 0.0063; binomial test) in both states (Fig. 5*E*). The knee peak frequencies did not differ between both states (Fig. 5*G*; first knee, $t_{(10)} = -0.35$; p = 0.7334; d = -0.11; second knee, $t_{(11)} = -1.15$; p = 0.2741; d = -0.33). Collectively, this set of findings demonstrates that spectral knees at ~5 Hz (wakefulness, 5.17 ± 0.17 Hz; anesthesia, 5.36 ± 0.45 Hz; mean \pm SEM) and ~75 Hz (wakefulness, 76.25 ± 1.63 Hz; anesthesia, 79.33 ± 2.00 Hz; mean \pm SEM) are brain state-independent and similar knees can be observed using depth electrodes (Study 1/3; compare Fig. 3*I*,*J*) as well as subdural grid electrodes (Study 2; Fig. 4*E*), implying that these might capture physiologic time constants that are inherent to the underlying neuronal population and not affected by anesthesia.

Discussion

Sleep is characterized by a variety of temporal regularities ranging from days (circadian rhythms) to hours (sleep cycles) and to (sub)seconds (e.g., sleep oscillations). In addition to these wellestablished temporal regularities, (1) the present findings provide evidence that neural timescales separate several 1/f decay processes that index the current brain state. (2) Specifically, the previously employed 30-50 Hz range (Gao et al., 2017; Lendner et al., 2020) largely (but not completely) avoids the spectral knees at 20 and 45 Hz. Hence, while this frequency range was adept at discriminating different sleep stages (Lendner et al., 2020; Kozhemiako et al., 2022), a range between 20 and 45 Hz might be even more optimal since it avoids the spectral knees all together. The inclusion of the low-frequency spectral knee in the estimation of the spectral slope also explains previous contradictory evidence of aperiodic activity in sleep (Colombo et al., 2019; Miskovic et al., 2019; Höhn et al., 2023; Rosenblum et al., 2023). Our results indicate that the presence of spectral knees should guide the parameter selection for estimation of the spectral slope, which might be brain state- and regionspecific. (3) Spectral knees predicted the systematic variation in the 1/f spectral slope between the MTL and PFC, which potentially reflects the distinct structural composition between the three- and six-layered cortex. (4) The proposed approximation did not misidentify oscillatory peaks as knees (such as spindles), demonstrating that this approach successfully separated aperiodic from oscillatory activity.

The neurophysiological basis of aperiodic activity

Recently, several analytical approaches were introduced to better characterize neural oscillations and aperiodic activity (Wen and Liu, 2016; Donoghue et al., 2020; Kosciessa et al., 2020). Previously, aperiodic activity has often been discarded as "noise," but emerging evidence suggests that it contains rich information (Voytek et al., 2015; Podvalny et al., 2021; Waschke et al., 2021; Pfeffer et al., 2022). Aperiodic activity exhibits a $1/f^{\chi}$ scaling behavior and is sometimes also termed nonoscillatory or scale-free activity (He et al., 2010; Donoghue et al., 2020).

To date, our understanding of the physiological mechanisms underlying aperiodic activity remains limited (Buzsáki et al., 2012; Kramer and Chu, 2023). Computational modeling has proposed that aperiodic activity could reflect neural excitability (Gao et al., 2017; Chini et al., 2021). This concept has sparked a recent surge of studies aiming to infer microscale properties from macroscale recordings (Ahmad et al., 2022). Emerging evidence, including in vivo calcium imaging (Lendner et al., 2023), optogenetic (Chini et al., 2021), and pharmacological (Colombo et al., 2019; Lendner et al., 2020) manipulations, has provided support for this notion. Most studies assume that aperiodic activity is only

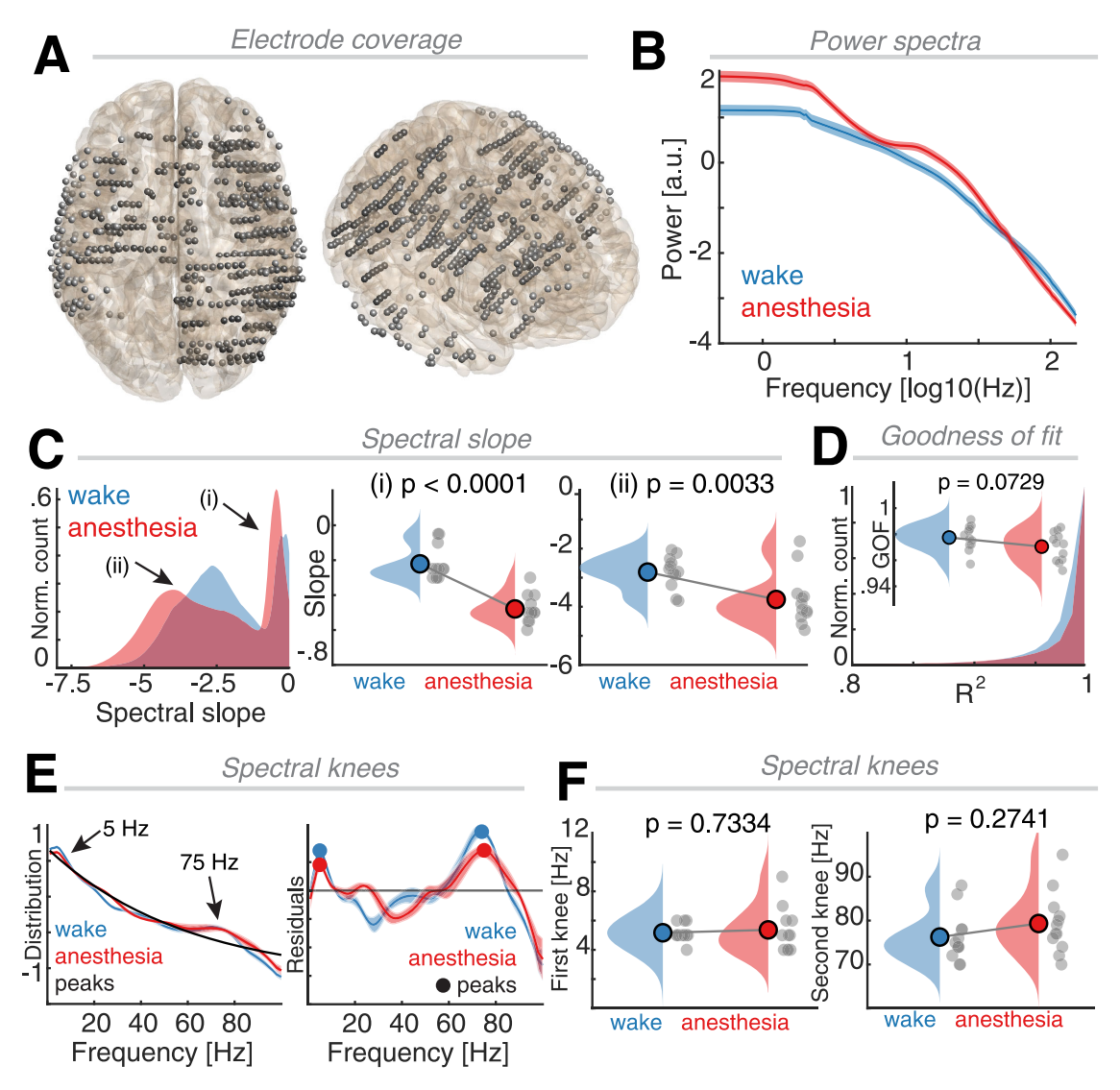


Figure 5. Modulation of intrinsic timescales during medically induced unconsciousness. *A*, Electrode coverage (*N* = 12; 632 bipolar pairs). *B*, Grand-average PSDs during wakefulness (blue) and propofol anesthesia (red). *C*, Left, Distribution of PSD slopes as obtained from iterative fitting in the wake state (blue) and under anesthesia (red) again reveals a bimodal distribution with flatter (*i*) and steeper (*ii*) spectral slopes (compare panel *F*). Center, Statistical quantification of the slope prior to the first knee indicated steeper PSD slopes during anesthesia. Right, Statistical quantification of the slope after the first knee further confirmed steeper PSD slopes during anesthesia. *D*, Overall goodness-of-fit did not differ between both states and, again, was close to 1, thus indicating that spectra can be well approximated by iterative spectral fitting. *E*, Left, Distribution of spectral knees during wakefulness (blue) and under anesthesia (red) relative to the exponential decay function (black). Right, Individual peak detection reveals consistent low- (~5 Hz) and high-frequency (~75 Hz) spectral knees. *F*, Statistical quantification of the low (left) and the high (right) knees demonstrated comparable estimates in both states.

characterized by one decay function with a fixed exponent. However, inconsistent state discrimination for varying frequency ranges (i.e., from 1 to 45 vs 30 to 45 Hz; Colombo et al., 2019; Miskovic et al., 2019; Lendner et al., 2020) implied that the 1/f spectral slope might not be uniform across the entire power spectrum.

Here, we demonstrate that the correlation of aperiodic activity with the sleep hypnogram varies across different frequency bands. This dependence is explained by the fact that the 1/f decay function is not constant. Iterative fitting revealed multiple and state- and region-dependent spectral knees that impact 1/f characteristics, i.e., a flatter spectrum in the MTL than PFC in the \sim 20–45 Hz range (compare Fig. 3). The limited spatial coverage of iEEG recordings cannot fully resolve whether the identified spectral knees can be detected everywhere in the cortex. In the present study, the majority of electrodes targeted the MTL and PFC, where we observed a surprising consistency across different

arousal states. It is critical to highlight that the precise peak frequency might depend on electrode placement as exemplified by differences between MTL and PFC in Study 1 (compare Fig. 31,J) or the variability that was observed in Study 2 (compare Fig. 4E), where large subdural electrode grid arrays were employed in contrast to the stereotactically placed depth electrodes. This regional dependency was further supported by the observation of flatter power spectra in subcortical regions, such as the basal ganglia (Wiest et al., 2023; Bush et al., 2024). Specifically, Bush et al. (2024) reported that subcortical regions do not exhibit an aperiodic knee, thus raising the intriguing possibility that knees may arise from the fine-grained anatomical structure of the cerebral cortex. Hence, the present findings may provide a window to infer (sub)cellular properties from large-scale, intracranial neural mass signals. Moreover, several recent studies demonstrated that low-frequency spectral knees can also be obtained from scalp EEG and may vary as a function of a sleep stage (Lendner et al., 2022; Ameen et al., 2024). However, the sensitivity of scalp EEG to muscle artifacts may preclude a reliable detection of high-frequency knees from scalp EEG.

The functional role of aperiodic neural timescales and its behavioral relevance

The concept of intrinsic neural timescales refers to the characteristic time constants over which neurons exhibit correlated activity (Voytek and Knight, 2015; Wolff et al., 2022). At the cellular level, timescales also refer to the decay constants of different receptors and ion channels (Fourcaud and Brunel, 2002; Moreno-Bote and Parga, 2005; Parisien et al., 2008). To date, it remains unclear how cellular- and population-based timescales are related.

Neural timescales are commonly regarded as hierarchically structured temporal integration windows (Murray et al., 2014). Conversely, it had been observed that the association cortex exhibits longer timescales than the sensory cortex (Gao et al., 2020; Cusinato et al., 2023). In line with these theoretical considerations, longer timescales in the prefrontal association cortex predicted better memory retention (Wasmuht et al., 2018; Gao et al., 2020) or integration of task-relevant information (Spitmaan et al., 2020; Zeraati et al., 2023).

Neural timescales are often inferred from the signal autocorrelation function, which typically identifies timescales in the range from 100 to 400 ms at the level of single-unit activity (Murray et al., 2014), while EEG timescales are \sim 10-fold faster (Gao et al., 2020). In the frequency domain, these timescales correspond to a spectral knee between \sim 0.4 and 1.6 Hz (unit activity) and \sim 4 and 16 Hz (EEG activity). However, in the frequency domain, spectral knees in human EEG have also been described as low as \sim 1–2 Hz (He et al., 2010; Gao et al., 2020) and up to \sim 20 Hz (Robinson et al., 2001, 2011; Chaoul and Siegel, 2021). Moreover, it has long been recognized that the power spectrum exhibits at least one additional characteristic bend at \sim 75 Hz (Miller et al., 2009).

To date, the physiology of these time constants is not very well understood, but it is likely that different timescales index distinct properties of the underlying population (Freeman and Zhai, 2009; Buzsáki et al., 2012). For example, certain timescales reflect static physical properties (e.g., synaptic currents or dendritic lowpass filtering; Robinson et al., 2001; Freeman and Zhai, 2009; Miller et al., 2009; Buzsáki et al., 2012). Here, we observed three timescales, which are well within the range of different receptor decay constants. AMPA receptor currents exhibit a decay function of ~2 ms (Hestrin et al., 1990; Sah et al., 1990), while GABA_A receptors have longer time constants of up to ~10 ms (Salin and Prince, 1996; Gupta et al., 2000; Fourcaud and Brunel, 2002). The longest time constants are reported for NMDA receptors with up to ~150 ms (Fourcaud and Brunel, 2002; Moreno-Bote and Parga, 2005; Parisien et al., 2008). While cellular properties do not directly map onto neural mass signals (Buzsáki et al., 2012; Einevoll et al., 2013), computation models may bridge the gap between cellular properties and large-scale neural signatures.

Here, we demonstrate relatively consistent spectral knees at \sim 1–5 Hz (\sim 30–160 ms timescale) and at \sim 65–75 Hz (\sim 2–3 ms timescale), which were also evident during pharmacologically induced unconsciousness and, therefore, may reflect physical properties. While we did observe highly comparable estimates across all three studies for low- and high-frequency knees, the current experiments cannot resolve their precise biophysical origin, and future experiments need to determine if these knees

might rather be the result of functional interactions. In contrast to the low- and high-frequency knees, timescales at \sim 20–45 Hz (\sim 4–8 ms) were brain state-dependent and region-specific (\sim 45 Hz more prevalent in the MTL, while \sim 20 Hz was more prevalent in the PFC).

Conclusions

Collectively, our findings provide compelling evidence that the electrophysiological power spectrum is shaped by multiple concurrent aperiodic processes. These processes are characterized by distinct time constants (knees), which act as systematic deflection points influencing the spectral slope. Notably, some of these time constants persist during general anesthesia, potentially indexing physical properties of the underlying neural population. Our results offer an explanation for why aperiodic activity within the frequency range of ~20-45 Hz serves as an effective discriminator of different sleep stages and reconcile seemingly contradictory findings, which were largely obtained from fits that encompassed either the high- (>45 Hz) or the low-frequency knee (<20 Hz), thus distorting the estimates. In sum, these findings demonstrate that various aspects of aperiodic activity, including timescales and decay functions, contain rich information about the current brain state.

References

Ahmad J, et al. (2022) From mechanisms to markers: novel noninvasive EEG proxy markers of the neural excitation and inhibition system in humans. Transl Psychiatry 12:467.

Ameen MS, Jacobs J, Schabus M, Hoedlmoser K, Donoghue T (2024) The temporal dynamics of aperiodic neural activity track changes in sleep architecture. 2024.01.25.577204 Available at: https://www.biorxiv.org/ content/10.1101/2024.01.25.577204v1 [Accessed June 28, 2024].

Bódizs R, Szalárdy O, Horváth C, Ujma PP, Gombos F, Simor P, Pótári A, Zeising M, Steiger A, Dresler M (2021) A set of composite, non-redundant EEG measures of NREM sleep based on the power law scaling of the Fourier spectrum. Sci Rep 11:2041.

Bush A, Zou JF, Lipski WJ, Kokkinos V, Richardson RM (2024) Aperiodic components of local field potentials reflect inherent differences between cortical and subcortical activity. Cereb Cortex 34:bhae186.

Buzsáki G, Anastassiou CA, Koch C (2012) The origin of extracellular fields and currents–EEG, ECoG, LFP and spikes. Nat Rev Neurosci 13:407–420. Chaoul AI, Siegel M (2021) Cortical correlation structure of aperiodic neuronal population activity. Neuroimage 245:118672.

Chini M, Pfeffer T, Hanganu-Opatz IL (2021) Developmental increase of inhibition drives decorrelation of neural activity. Available at: https://www.biorxiv.org/content/10.1101/2021.07.06.451299v1 [Accessed September 20, 2021].

Colombo MA, et al. (2019) The spectral exponent of the resting EEG indexes the presence of consciousness during unresponsiveness induced by propofol, xenon, and ketamine. Neuroimage 189:631–644.

Cusinato R, Alnes SL, van Maren E, Boccalaro I, Ledergerber D, Adamantidis A, Imbach LL, Schindler K, Baud MO, Tzovara A (2023) Intrinsic neural timescales in the temporal lobe support an auditory processing hierarchy. J Neurosci 43:3696–3707.

Donoghue T, et al. (2020) Parameterizing neural power spectra into periodic and aperiodic components. Nat Neurosci 23:1655–1665.

Einevoll GT, Kayser C, Logothetis NK, Panzeri S (2013) Modelling and analysis of local field potentials for studying the function of cortical circuits. Nat Rev Neurosci 14:770–785.

Fourcaud N, Brunel N (2002) Dynamics of the firing probability of noisy integrate-and-fire neurons. Neural Comput 14:2057–2110.

Freeman WJ, Zhai J (2009) Simulated power spectral density (PSD) of background electrocorticogram (ECoG). Cogn Neurodyn 3:97–103.

Gao R, Peterson EJ, Voytek B (2017) Inferring synaptic excitation/inhibition balance from field potentials. Neuroimage 158:70–78.

Gao R, van den Brink RL, Pfeffer T, Voytek B (2020) Neuronal timescales are functionally dynamic and shaped by cortical microarchitecture. Elife 9: e61277.

- Gerster M, Waterstraat G, Litvak V, Lehnertz K, Schnitzler A, Florin E, Curio G, Nikulin V (2022) Separating neural oscillations from aperiodic 1/f activity: challenges and recommendations. Neuroinform 20:991–1012.
- Gupta A, Wang Y, Markram H (2000) Organizing principles for a diversity of GABAergic interneurons and synapses in the neocortex. Science 287:273–278
- He BJ, Zempel JM, Snyder AZ, Raichle ME (2010) The temporal structures and functional significance of scale-free brain activity. Neuron 66:353–369
- Hestrin S, Sah P, Nicoll RA (1990) Mechanisms generating the time course of dual component excitatory synaptic currents recorded in hippocampal slices. Neuron 5:247–253.
- Höhn C, Hahn MA, Lendner JD, Hoedlmoser K (2023) Spectral slope and Lempel-Ziv complexity as robust markers of brain states during sleep and wakefulness. 2022.09.10.507390 Available at: https://www.biorxiv. org/content/10.1101/2022.09.10.507390v3 [Accessed November 1, 2023].
- Kosciessa JQ, Grandy TH, Garrett DD, Werkle-Bergner M (2020) Single-trial characterization of neural rhythms: potential and challenges. Neuroimage 206:116331.
- Kozhemiako N, Mylonas D, Pan JQ, Prerau MJ, Redline S, Purcell SM (2022) Sources of variation in the spectral slope of the sleep EEG. eNeuro 9: ENEURO.0094-22.2022.
- Kramer MA, Chu CJ (2023) The 1/f-like behavior of neural field spectra are a natural consequence of noise driven brain dynamics. 2023.03.10.532077 Available at: https://www.biorxiv.org/content/10.1101/2023.03.10.532077v5 [Accessed November 1, 2023].
- Lendner JD, et al. (2023) Human REM sleep recalibrates neural activity in support of memory formation. Sci Adv 9:eadj1895.
- Lendner JD, Helfrich RF, Mander BA, Romundstad L, Lin JJ, Walker MP, Larsson PG, Knight RT (2020) An electrophysiological marker of arousal level in humans. Elife 9:e55092.
- Lendner JD, Mander BA, Schuh-Hofer S, Schmidt H, Knight RT, Walker MP, Lin J, Helfrich RF (2022) Human REM sleep controls neural excitability in support of memory formation. 2022.05.13.491801 Available at: https:// www.biorxiv.org/content/10.1101/2022.05.13.491801v1 [Accessed June 28, 2024].
- Miller KJ (2019) A library of human electrocorticographic data and analyses. Nat Hum Behav 3:1225–1235.
- Miller KJ, Sorensen LB, Ojemann JG, Den Nijs M (2009) Power-law scaling in the brain surface electric potential. PLoS Comput Biol 5:e1000609.
- Miskovic V, MacDonald KJ, Rhodes LJ, Cote KA (2019) Changes in EEG multiscale entropy and power-law frequency scaling during the human sleep cycle. Hum Brain Mapp 40:538–551.
- Moreno-Bote R, Parga N (2005) Simple model neurons with AMPA and NMDA filters: role of synaptic time scales. Neurocomputing 65–66: 441–448.
- Murray JD, et al. (2014) A hierarchy of intrinsic timescales across primate cortex. Nat Neurosci 17:1661–1663.
- Nir Y, de Lecea L (2023) Sleep and vigilance states: embracing spatiotemporal dynamics. Neuron 111:1998–2011.
- Oostenveld R, Fries P, Maris E, Schoffelen J-M (2011) Fieldtrip: open source software for advanced analysis of MEG, EEG, and invasive electrophysiological data. Comput Intell Neurosci 2011:156869.
- Parisien C, Anderson CH, Eliasmith C (2008) Solving the problem of negative synaptic weights in cortical models. Neural Comput 20:1473–1494.
- Pfeffer T, Keitel C, Kluger DS, Keitel A, Russmann A, Thut G, Donner TH, Gross J (2022) Coupling of pupil- and neuronal population dynamics reveals diverse influences of arousal on cortical processing. Elife 11: e71890.
- Podvalny E, King LE, He BJ (2021) Spectral signature and behavioral consequence of spontaneous shifts of pupil-linked arousal in human (Obleser J, Gold JI, de Gee JW, David S, eds). Elife 10:e68265.
- Rasch B, Born J (2013) About sleep's role in memory. Physiol Rev 93:681–766.

- Raut RV, Snyder AZ, Raichle ME (2020) Hierarchical dynamics as a macroscopic organizing principle of the human brain. Proc Natl Acad Sci U S A 117:20890–20897.
- Rechtschaffen A, Kales A (1968) A manual of standardized terminology, techniques, and scoring systems for sleep stages of human subjects.
- Robinson PA, Phillips AJK, Fulcher BD, Puckeridge M, Roberts JA (2011) Quantitative modelling of sleep dynamics. Philos Trans A Math Phys Eng Sci 369:3840–3854.
- Robinson PA, Rennie CJ, Wright JJ, Bahramali H, Gordon E, Rowe DL (2001) Prediction of electroencephalographic spectra from neurophysiology. Phys Rev E 63:021903.
- Rosenblum Y, Esfahani MJ, Adelhöfer N, Zerr P, Furrer M, Huber R, Steiger A, Zeising M, Horváth CG, Schneider B, Bódizs R, Dresler M (2023) Fractal cycles of sleep: a new aperiodic activity-based definition of sleep cycles. 2023.07.04.547323 Available at: https://www.biorxiv.org/content/10.1101/2023.07.04.547323v1 [Accessed November 1, 2023].
- Sah P, Hestrin S, Nicoll RA (1990) Properties of excitatory postsynaptic currents recorded in vitro from rat hippocampal interneurones. J Physiol 430: 605–616.
- Salin PA, Prince DA (1996) Spontaneous GABAA receptor-mediated inhibitory currents in adult rat somatosensory cortex. J Neurophysiol 75:1573–1588.
- Shinn M, et al. (2023) Functional brain networks reflect spatial and temporal autocorrelation. Nat Neurosci 26:867–878.
- Siegel JM (2011) REM sleep: a biological and psychological paradox. Sleep Med Rev 15:139.
- Soltani A, Murray JD, Seo H, Lee D (2021) Timescales of cognition in the brain. Curr Opin Behav Sci 41:30–37.
- Spitmaan M, Seo H, Lee D, Soltani A (2020) Multiple timescales of neural dynamics and integration of task-relevant signals across cortex. Proc Natl Acad Sci U S A 117:22522–22531.
- Stolk A, Griffin S, van der Meij R, Dewar C, Saez I, Lin JJ, Piantoni G, Schoffelen J-M, Knight RT, Oostenveld R (2018) Integrated analysis of anatomical and electrophysiological human intracranial data. Nat Protoc 13:1699–1723.
- Stouffer SA, Suchman EA, De Vinney LC, Star SA, Williams RM (1949) Studies in social psychology in world war II. Vol. I: the American soldier: adjustment during army life. Princeton, NJ: Princeton University Press.
- van Schalkwijk FJ, Weber J, Hahn MA, Lendner JD, Inostroza M, Lin JJ, Helfrich RF (2023) An evolutionary conserved division-of-labor between archicortical and neocortical ripples organizes information transfer during sleep. Prog Neurobiol 227:102485.
- Voytek B, Knight RT (2015) Dynamic network communication as a unifying neural basis for cognition, development, aging, and disease. Biol Psychiatry 77:1089–1097.
- Voytek B, Kramer MA, Case J, Lepage KQ, Tempesta ZR, Knight RT, Gazzaley A (2015) Age-related changes in 1/f neural electrophysiological noise. J Neurosci 35:13257–13265.
- Waschke L, Donoghue T, Fiedler L, Smith S, Garrett DD, Voytek B, Obleser J (2021) Modality-specific tracking of attention and sensory statistics in the human electrophysiological spectral exponent. Elife 10:e70068.
- Wasmuht DF, Spaak E, Buschman TJ, Miller EK, Stokes MG (2018) Intrinsic neuronal dynamics predict distinct functional roles during working memory. Nat Commun 9:3499.
- Wen H, Liu Z (2016) Separating fractal and oscillatory components in the power spectrum of neurophysiological signal. Brain Topogr 29:13–26.
- Wiest C, et al. (2023) The aperiodic exponent of subthalamic field potentials reflects excitation/inhibition balance in parkinsonism. Elife 12:e82467.
- Wolff A, Berberian N, Golesorkhi M, Gomez-Pilar J, Zilio F, Northoff G (2022) Intrinsic neural timescales: temporal integration and segregation. Trends Cogn Sci 26:159–173.
- Zeraati R, Shi YL, Steinmetz NA, Gieselmann MA, Thiele A, Moore T, Levina A, Engel TA (2023) Intrinsic timescales in the visual cortex change with selective attention and reflect spatial connectivity. Nat Commun 14:1858.